The additive manufacture processing and machinability of CrMnFeCoNi high entropy alloy

Przemyslaw Litwa [a], Everth Hernandez-Nava [b], Dikai Guan [b,c], Russell Goodall [b,*], Krystian K. Wika [a]

[a] Nuclear Advanced Manufacturing Research Centre, the University of Sheffield, Brunel Way, Rotherham S60 5WG, UK
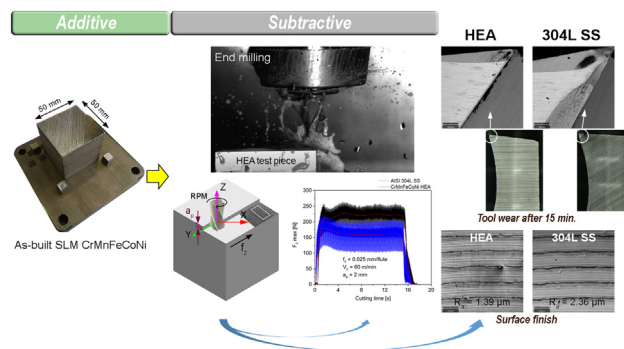[b] Department of Materials Science & Engineering, the University of Sheffield, Sir Robert Hadfield Building, Portobello St, Sheffield S1 3JD, UK
[c] The Henry Royce Institute, Sir Robert Hadfield Building, Sheffield, S1 3JD, UK

HIGHLIGHTS

- CrMnFeCoNi has been processed by SLM following a design of experiments (DoE) achieving high density.
- No local segregation was found in as-built material keeping the homogeneity of the high entropy composition.
- CrMnFeCoNi has been successfully machined following a parametric approach achieving minimum surface roughness and defects.
- The machinability design space and tool wear have been fully characterised.

GRAPHICAL ABSTRACT

ARTICLE INFO

ABSTRACT

We report a study of the machining characteristics of a High Entropy Alloy, CrMnFeCoNi (Cantor's Alloy). The alloy in powder form is first used to Additively Manufacture a relatively large block by Selective Laser Melting. This block provides the material for a parametric study of the machining response in comparison to a reference AISI 304L stainless steel, both in terms of the surface finish obtained for different machining parameters, and the tool wear. It was found that the CrMnFeCoNi alloy has in fact better machinability than the AISI 304L stainless steel, and indications from the machined surface are that this is due to the plastic behaviour in this alloy, with good, but not excessive, strength, and significant ductility. While this behaviour may not be replicated in all HEAs, it shows that alloys with good machinability can be found in this class, and that early assessment of machinability can help guide alloy design activities.

© 2020 The Author(s). Published by Elsevier Ltd. This is an open access article under the CC BY license (http://creativecommons.org/licenses/by/4.0/).

1. Introduction

In the search for new metallic materials for applications, the type of alloys known variously as High Entropy Alloys (HEAs), Complex Concentrated Alloys (CCAs) or multiprincipal component alloys is receiving much attention [1]. This is motivated by the fact that the design philosophy of these alloys can lead to exploration of new combinations of elements, and the potential to discover new alloys of many types [2], and that some alloys identified in this way have unusual and attractive property combinations [3] [4]. A good combination of mechanical properties and corrosion resistance make them potential substitute candidates for nickel-based superalloys, such as Inconel 718 or Haynes 230 for applications demanding high specific strength at high temperatures [5].

The feature that distinguishes HEAs from conventional alloys based on a single principal element in each case, is that HEAs can maintain their potentially favourable properties over a relatively wide range of

* Corresponding author.
E-mail address: r.goodall@sheffield.ac.uk (P. Litwa).

mixing compositions. In conventional alloy design, the properties depend very strongly on the solubility limits of individual elements and proportions of the phases, both of which can be influenced by temperature and pressure. In HEAs, although these factors still exist, the increased number of variables, and perhaps the role of entropy in mixing, can allow more variation in composition without entering a new phase field. Also, the practical use of conventional alloys in many situations is often limited due to formation of intermetallic compounds which are inherently brittle. The phase stability of HEAs is of significant importance in determining their mechanical properties. The stability of a single phase solid solution depends on the entropic contribution to the Gibbs free energy [6]. In some cases, this mixing entropy contribution could be comparable to the formation enthalpies of intermetallic compounds and thus suppress their formation [7] [8].

In this study, the Additive Manufacture (AM) processing by Selective Laser Melting (SLM) and post-machining of CrMnFeCoNi are reported. This alloy was chosen as it was one of the first reported (Cantor's alloy [9]), and is thus one of the most widely characterised. The properties that it displays are relatively typical for HEAs, without being the most extreme found to date; it has a good combination of strength and ductility achieved with, for most processing histories, a single phase solid solution microstructure.

There is still a lot of development that is required before these alloys find widespread applications however. There are areas where the fundamental physical metallurgy of such systems is not fully understood, and a range of engineering issues, important for design and application, that are not yet adequately tested. These include the response of these alloys to different forms of primary and secondary processing (possibly changing their properties through induced alterations to their microstructure), and finishing operations such as machining. Additive Manufacturing enables the fabrication of net or near net shape components, however, it frequently produces poor surface finish due to the layer-by-layer building strategy and the associated stair stepping effect [10]. The porosity and microstructural non-homogeneities that result from rapid solidification of an alloy, occurring due to the sharp temperature gradients, have a detrimental effect on the machinability and surface integrity of additively manufactured components [11]. Therefore, further post processing of parts is required. The determination of the cutting forces in machining needs to be investigated and revised, not only to improve the surface finish, but also for optimum fixturing and aligning of complex-shaped components. Considering recent developments of HEAs and the future prospects of additively manufactured parts for different applications it is necessary to familiarise those who may potentially design or manufacture such alloys with the machinability of HEAs. Machinability assessment of HEAs is especially important to determine the proper machining procedures to post process parts fabricated with AM.

Among the various HEAs, the most thoroughly investigated multicomponent alloys are based on a single-phase CrMnFeCoNi alloy [12]. For nearly two decades, since the equatomic version of this alloy (one of the earliest HEAs) was reported [9], there has been a very limited number of studies examining the machinability of HEAs in the literature. For example, a recent publication by Huang et al. [13] reports the surface finish and tool wear in turning of $Al_{80}Li_5Mg_5Zn_5Cu_5$. This alloy is in many ways HEA-like, having multiple components, though the dominant content of aluminium would mean it would not meet most of the established definitions. Most of the available literature is concerned with investigation of the impact of primary manufacturing processes on the structure and properties of HEAs. The influence of process parameters and post-processing heat treatment on microstructure and phase stability in HEAs has been studied [14], also to give a better understanding of mechanical behaviour and corrosion resistance at elevated temperatures [15,16]. Further, some attempts were made to investigate the feasibility of fibre laser welding of thin section HEAs

made by ingot metallurgy [17], and alternatively after subsequent rolling [18]. Electric arc and laser welding of HEAs resulted in a lower hardness in the welded region compared to friction stir welding [19].

Machining is indispensable for the manufacturing of metal components enabling holes to be made, slots and other more complex features to be created. In general, the machinability of a material mainly depends on the microstructure and properties resulting from the chemical composition and processing conditions. Different microstructures affect the hardness of a material and thermal conductivity, both of which might lead to different machining characteristics. For example, the low thermal conductivity and high hardness of nickel-based superalloys [20], additionally affected by the high volume fraction of carbides frequently present, pose challenges for machining processes, causing such problems as premature tool failure and poor chip control, which create chatter (i.e. resonant vibration) and result in poor surface finish [21]. Also, high work hardening in metals such as Duplex stainless steels, produces higher cutting forces and high contact pressures at the tool-chip interface resulting in increased cutting temperature, with poor machinability [22]. Therefore, it could be expected that HEAs, with their extremal properties of very high strength, may present challenges to machining. If this is the case, then understanding this behaviour and the limitations now, rather at a later stage of product and component development, will be valuable.

With powder-bed fusion Additive Manufacture (AM) becoming an important processing route in recent years, a potential alternative to scale up materials into the manufacturing sector is offered. With limitations on surface finish [23] and resolution [24] however, an opportunity to address these challenges, prior parts get into service, requires an appropriate study on materials and processes. It is therefore desirable to investigate the machining on as-built AM material to pair up the benefits of both processing routes.

In this study, CrMnFeCoNi alloy is tested in comparison with a reference AISI 304L stainless steel regarding its machinability and the results demonstrate that this particular HEA can be machined successfully by standard machining methods, and that the characteristics are comparable to, or more favourable than the stainless steel used as a baseline.

2. Materials and methods

2.1. Material processing by selective laser melting

The multicomponent CrMnFeCoNi alloys were fabricated by selective laser melting (SLM) using a Renishaw 125 system and gas atomised pre-alloyed powder with a 15 — 45 μm particle size distribution as feedstock powder for SLM. The typical chemical composition of the powder was measured using inductively coupled plasma optical emission spectroscopy (ICP-OES) technique reporting a composition of $Cr_{18.7}Mn_{19.7}Fe_{19.4}Co_{21.0}Ni_{21.2}$ (at. %). The SLM processing parameters were selected following a full factorial central composite design (CCC) design at two levels; point distance (20 — 100 μm) and laser exposure time (30 — 120 μs). Thirteen cuboid samples with dimensions of $10 \times 10 \times 6$ mm on a substrate were initially fabricated, depositing 30 μm thick layers using constant hatch spacing (50 μm) and maximum beam power of 200 W (see Table 1). Density measurements of fabricated samples were performed by the hydrostatic weighing method. In addition, metallographic preparation of high density samples was performed for X-ray diffraction (XRD) analysis and analysis of porosity using optical microscopy. XRD measurements were performed using a Siemens D5000 X-ray diffractometer under the standard Bragg-Brentano configuration using K_α radiation with a wavelength, λ_{Cu}, of 1.54 Å. A design space for parameter optimisation in additive manufacture of CrMnFeCoNi alloy was explored by which the optimal configuration of parameters was found. The SLM processing of the part for machinability studies, a block of $50 \times 50 \times 50$ mm (as described in section 2.2) was performed using laser power 200 W with a point distance

Table 1
The SLM process parameters used for AM of CrMnFeCoNi samples.

Specific aims Process parameters	Manufacturing feasibility	Manufacturing & Machining feasibility
Layer thickness, [μm]	30	30
Laser power, [W]	200	200
Hatch distance, [μm]	50	50
Point distance, μm]	20 — 100	43
Laser exposure time, [μs]	30 — 120	32
Scanning strategy	Alternating with 60°	Alternating with 60°
Substrate set temperature, [°C]	20	20

Table 2
Chemical composition of AISI 304L austenitic stainless steel.

Elements (wt%)								
C	Si	Mn	P	S	Cr	Ni	N	Co
0.024	0.301	1.885	0.035	0.0016	18.010	8.036	0.0822	0.158
Cu	**Mo**	**Nb**	**Ti**	**Fe**				
0.434	0.426	0.003	0.003	Bal.				

of 43 μm and time of exposure 32 μs. This set of parameters is discussed in the following section. Complementary Vickers hardness measurements were obtained using a Struers Durascan system, with loading conditions of 1 kg load for 5 s of dwell time in a grid of 5 × 4 indentations with 1 mm spacing.

2.2. Machining trials

After the HEA block was manufactured, skimming was performed to a depth of 1 mm from the top and side faces on the XYZ Hybrid Mill SMX 3500 machine tool to final dimensions of 48 × 48 × 49 mm. This was to minimise the effect of near-surface higher potential porosity/flaws on machining performance.

Machining trials were performed on the Hartford LG-500 CNC Vertical Machining Centre. The test piece was clamped with a Hilma MC-P 125 Z concentring clamping vice using fixing screws to fasten the jaws together as shown in Fig. 1.

The vice was mounted to a Kistler Type 9255C dynamometer for cutting force measurement. The resultant forces were calculated from the square root of the total of the squares of the individual force components. The maximum values of a resultant cutting force were noted and taken for further evaluation. Machinability of CrMnFeCoNi HEA in the as-built SLM condition was compared and contrasted to a commonly known and easily available AISI 304L austenitic stainless steel. The steel was received as a hot rolled block (48 × 48 × 90 mm) of the nominal chemical composition presented in Table 2. AISI 304L is generally recognised to have good machinability, and it was chosen here only to provide manufacturers with a reference for the machining performance of CrMnFeCoNi HEA in relation to a reference 304L stainless steel material. It was not the intention to compare and directly asses the composition and microstructure resulting from the manufacturing of these two materials, but to contextualise the machinability of the HEA in contrast to a widely known material.

2.2.1. Design of experiments

Machinability of CrMnFeCoNi HEA was investigated in climb milling trials under various cutting conditions using HOCUT 795N soluble oil as coolant at 7% concentration. The cutting tool used was a 10 mm diameter uncoated 4-flute solid carbide end mill provided by Guhring (GUH03198010.000). All the tools were mounted in a Sandvik Coromant 930-BB40-HD-20-088 with the fixed tool stick out from the tool holder. The runout of the tool was checked at the cutting edges on the mounted tool with a Zoller Smile 420 tool presetter to confirm whether it is within manufacturer's tolerances (maximum of 4 μm at 25 mm distance from the chuck).

A Central Composite Face (CCF), three factors at two-level, design was used in machining optimisation trials for HEA material. The total number of 34 randomised runs (14 runs in design, three centre points and one replicate), were carried out. The cutting edge of each cutting tool was inspected for any damage and flank wear before each run. Each cutting tool was used in no more than three experimental runs, providing the observed tool wear after each cutting pass was not greater than 50 μm. Table 3 summarises the input factors and their corresponding levels used in the DOE for HEA.

The response factors in the DOE were cutting forces and surface roughness (Ra). In addition, a smaller 2-level design with two factors at constant depth of cut of 2 mm and varying feed rate and cutting speed (the same low and high level values as in case of HEA DOE as seen in Table 3) was created. This was to compare the effect of input factors (feed rate and cutting speed) on the response factors (surface roughness and cutting forces) in end milling of a reference material (AISI 304L SS).

The surface roughness was measured along the feed direction with the SJ-410 series skidless measurement system from Mitutoyo. The arithmetic average of the roughness profile (R_a) was used for analysis of the surface finish.

A 5 mm thick strip of the machined test piece was first cut off using wire electrical discharge machine (EDM). Then, small rectangular samples (10 × 6 × 5 mm) were cut off for surface texture analysis. The Keyence VK-X260k series 3D laser scanning confocal microscope was used to analyse the sample's surface. A Phenom XL scanning electron microscope (SEM) was used for surface topography imaging. The
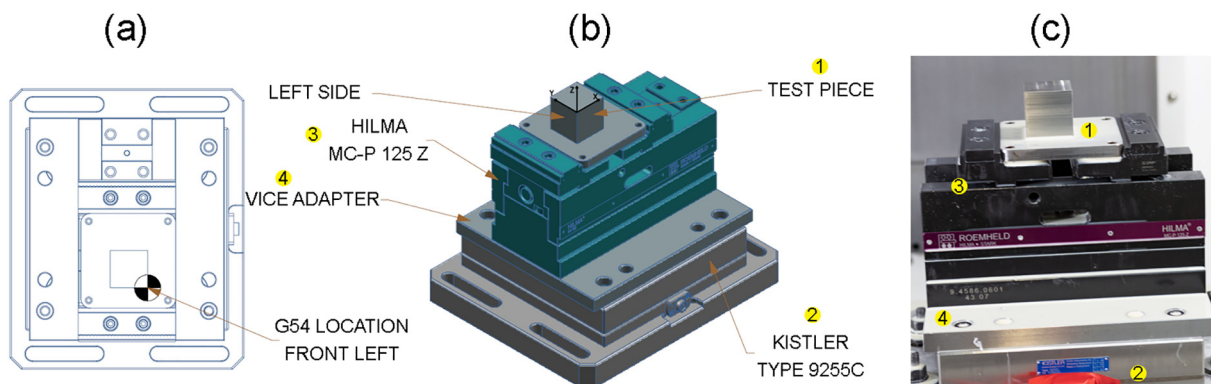

Fig. 1. (a) Machine setup with a datum reference. (b, c) Mounted fixture-test piece assembly.

Table 3
Summary of the cutting conditions used in the DOE for HEA material.

Factor	Feed rate, f_z [mm/flute]	Cutting speed, V_c [m/min]	Axial depth of cut, a_p [mm]
Low level	0.025	60	1
Medium level	0.033	87.5	1.5
High level	0.040	115	2

samples were mounted into an epoxy resin with a hot mounted press. The cross sections of samples were then prepared for microhardness measurements and microstructure analysis. Microstructural analysis was performed on samples etched electrochemically in a 60:40 mixture of nitric acid and distilled water at about 1.5 V and for up to 60 s. The Vickers microhardness was measured using a TUKON 2500 automated hardness tester under a load of 50 g with a dwell time of 15 s. The microhardness measurements are the average values of five independent measurements.

2.2.2. Tool wear trials

Tool wear trials were performed to compare machining performance of CrMnFeCoNi HEA with AISI 304L stainless steel as a reference material. The cutting tools and machine setup used for tool wear trials were the same as described in section 2.2. Tool wear measurements were carried out parallel to the cutting tool axis and in a perpendicular direction to the cutting edge according to ISO 8688-2 [25]. The width of cut in tool wear trials was kept at 4 mm (40% tool engagement) to not overload the tool and prevent excessive and uncontrolled tool edge fracturing during end milling. In order to directly compare and contrast machinability of CrMnFeCoNi HEA and stainless steel 304L, a single set of cutting conditions was selected for both materials (Table 4). The progression of flank wear for both materials was measured using a Nikon Shuttlepix P-400R optical microscope until the tool reached the flank wear criterion of $V_B = 200$ μm.

2.3. Post machining characterisation

After machining trials, cross sections of the material at the surface were prepared and imaged in Electron Backscatter Diffraction (EBSD), in order to explore the microstructure of the samples and changes occurring near-surface due to deformation. The samples were mounted into a large slotted sample holder (dimensions Ø32 x 15 mm, 6 mm wide by 6 mm deep slot) and were fixed by two side screws. The cross sections of samples were then ground and polished using SiC paper, 1 μm, 0.25 μm diamond suspension, 40 nm OPS suspension. EBSD was performed using a JEOL JSM-7900 field emission gun SEM fitted with Oxford Instruments Symmetry EBSD detector. The EBSD scanning accelerated voltage was 15 kV, probe current was 10 nA and step size was 0.15 μm. The EBSD data were analysed via using HKL CHANNEL5 software.

3. Results and discussion

3.1. Optimisation of SLM process parameters

A series of samples were fabricated according to the methods previously mentioned in section 2.1. Evaluation of processing parameters on

Table 4
Summary of the cutting conditions used in tool wear trials.

V_c [m/min]	f_z [mm/flute]	a_p [mm]	a_e [mm]	Material removal rate [mm³/min]
60	0.025	2	40	197

manufactured samples, shown in Fig. 2, was performed by measuring density achieved on each sample, and plotted in contours as the output parameter, see Fig. 3.

Overall, a fair level of density was found in all processed samples, achieving a maximum density of 7.806 g/cm³ (a relative density of 96.9%) for a point distance and beam exposure of 32 μm and 43 μs respectively, with an energy per unit volume of 211 J/mm³ (layer thickness and hatch offset above mentioned). This corresponds to the highest density region on a surface plot in Fig. 3.

From our process window, it can be seen that high porosity is developed for relative high point distances at low values of beam exposure (Fig. 2(b) and Fig. 3), with optimum density at lower point distances for a fairly wide range of beam exposure. This can be seen as the heat source creating an optimal melt-pool that fully closes gaps (pores) if worked at correct distance. Increasing exposure seems to work for a more reduced range of point distance however. Discussing the origin of pores in SLM parts scape the scope of the present study. It can be mentioned however that porosity may be created from over exposure of the heat source (keyhole) [26] and/or fluid dynamics of the melt pool [27], apart from lack of fusion due to inefficient energy input [28]. It is therefore sensible to suggest that the minimum point distance and beam exposure selected here, perform in such a way that beam parameters achieved high density in CrMnFeCoNi.

Properties of density, hardness and structural phase agree, to a fair extent, to previous results by Brif et al. [29] on a similar HEA, FeCoCrNi, with average microhardness of 228 ± 9 HV and a single phase structure as shown in Fig. 4.

In addition, X-ray diffraction showed a single FCC phase structure and a lattice parameter of 3.591A. Previous studies [30], agree this value to a fair extent (3.596–3.602 A) for a HEA processed with a continuous laser AM equipment using a range of energy input (59–185 J/mm³). In their study, the authors processed their material obtaining a range of lattice parameters attributing differences to variation on beam energy, reporting that higher input correlate to a decrease in lattice parameters due to evaporation losses of one of their elemental components. In this work, the chosen set of parameters did report a manganese loss, commented on in section 3.4, agreeing that both values fall on reported ends found in literature [30].

3.2. Cutting forces and tool wear

From the DOE optimisation trials (Fig. 5 and Fig. 6(a)) it was found that the feed rate, followed by the axial depth of cut, have the most significant influence on the cutting forces in milling of CrMnFeCoNi HEA. The force values increase with increased feed rate and are higher at increased axial depth of cut, as would be expected. Fig. 5 presents contour plots based on the multiple linear regression (MLR) model obtained for measured cutting forces. The R^2 and Q^2 values were 0.883 and 0.724, respectively, at a confidence level of 95%.

Fig. 5 shows that generally the resultant force decreases with a decrease in feed rate and depth of cut. However, for high cutting speeds and low feed rate, the cutting forces are lower regardless of the depth of cut. Higher cutting speeds typically result in an increase of heat generated in the cutting zone, which in turn might lead to material thermal softening of the test piece, and might play a role in controlling residual stress levels. It is likely that the cutting temperature (for high cutting speeds) will be higher for the AISI 304L stainless steel reference material than in CrMnFeCoNi HEA. Nasr et al. [31] noted that some thermal properties of the test piece play a key role in controlling the cutting process, and the test piece thermal conductivity (or diffusivity) is an important one of these, due to its role in influencing the distribution of thermal energy in the test piece. The measured thermal conductivity with the laser flash method of SLM manufactured CrMnFeCoNi HEA is about 24 W/mK at lower temperatures, gradually increasing up to 34 W/mK at ~873 K. Jin et al. [32], reported slightly lower thermal conductivity value of CrMnFeCoNi, 13.7 W/mK at 300 K, which is comparable with AISI
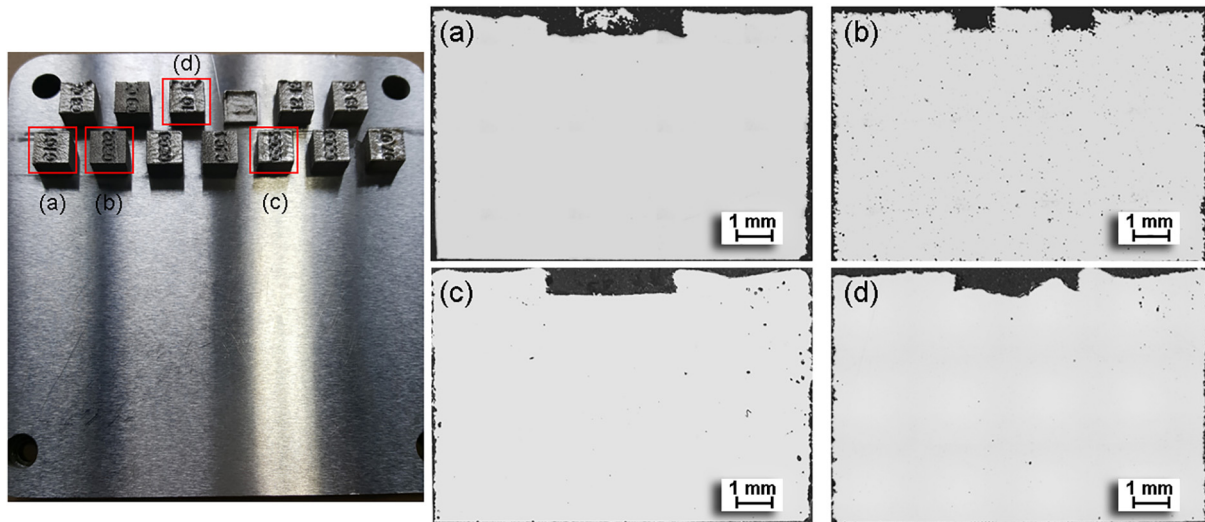
Fig. 2. Manufactured samples and examples of cross-section surfaces including SLM parameters and density: (from left) as-built CrMnFeCoNi cuboids (a) ExpT = 43 µs, pd. = 32 µm (7.806 g/cm³, 96.9%), (b) ExpT = 43 µs, pd. = 88 µm (6.967 g/cm³, 86.5%), (c) ExpT = 107 µs, pd. = 32 µm (7.684 g/cm³, 95.4%) and (d) ExpT = 107 µs, pd. = 88 µm (7.658 g/cm³, 95.1%).
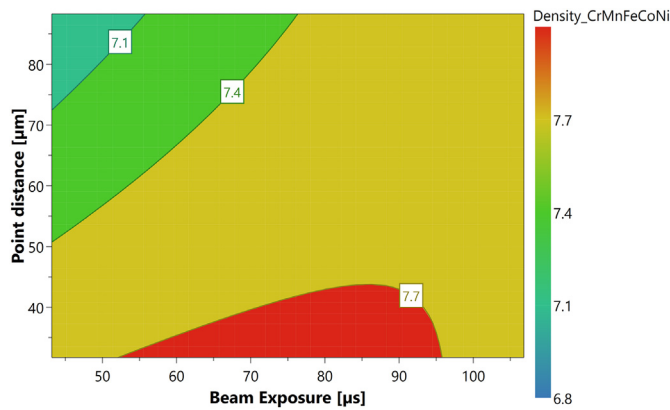

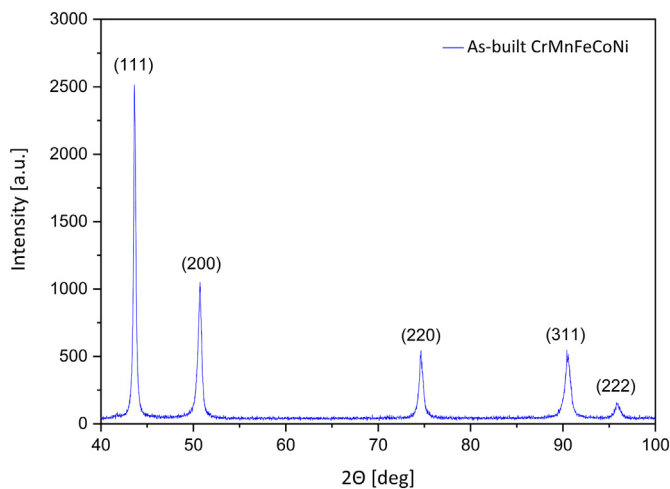**Fig. 3.** The density contour plot of the as-fabricated samples under various processing parameters.

Fig. 4. X-ray diffraction pattern of as-built CrMnFeCoNi alloy showing peaks of a single-phase face-centered cubic (fcc) structure.

304L stainless steel (13 W/mK at room temperature with a further increase to 23 W/m.K at 900 K) [33]. The higher thermal conductivity of CrMnFeCoNi HEA investigated here, than that of austenitic stainless steel would help to improve the heat dissipation and consequently lead to a decrease in the cutting temperature in the HEA sample.

Force measurements were also performed for AISI 304L stainless steel in order to compare and contrast the results with the SLM processed HEA. The resultant forces during machining of the reference material and CrMnFeCoNi HEA are shown by the contour plot in Fig. 7. Fig. 8 presents the resultant cutting force distributions along the cut.

From Fig. 6, the maximum forces in machining of AISI 304L stainless steel were generally higher than in CrMnFeCoNi HEA. The cutting forces increase with increasing feed promoting the plastic deformation and heat generation in the cutting zone. From Fig. 7 it can be seen that the milling process is stable only at the lowest cutting speed used in the experiments (Fig. 7(a, b)). The maximum cutting forces nearly doubled as feed rate increased from 0.025 mm/flute to 0.04 mm/flute (Fig. 7(b)). Further increase in the spindle speed caused rapid tool wear, which consequently resulted in high maximum cutting forces (Fig. 7(c)). In the worst-case scenario, the tool was damaged within a few seconds from the start of cutting. The cutting edges of the flutes on the tool were damaged, and this promoted further rubbing of the surface by a worn tool; evidence for this behaviour can be seen in Fig. 7(d). Machining of AISI304L at high cutting conditions is not stable and certainly, results are not comparable. Also, non-homogenous microstructure located in the cutting zone and the presence of precipitates in the parent material may cause a decrease in ductility during machining of AISI 304L stainless steel. Therefore, a contour plot in Fig. 6(b) presents the results based only on repeated trials of an experiment until when no tool damage occurred. Similar behaviour was not observed during machining of CrMnFeCoNi HEA with the same cutting conditions as for AISI 304L stainless steel (Fig. 7(e - h)). During the machining trials in HEA alloy a steady state conditions were observed, which can also be seen in the insets to Fig. 7. Due to this, it was possible to assess that the test piece had generally uniform composition and properties throughout its volume. This demonstrates that the SLM process was able to operate uniformly to produce a consistent HEA sample of relatively large size. Such large HEA samples have not been characterised before, to the authors' knowledge. For CrMnFeCoNi HEA, the cutting forces do not exceed the reasonable maximum force limit encountered in machining the reference material when the milling process is stable (Fig. 7(a, b)).
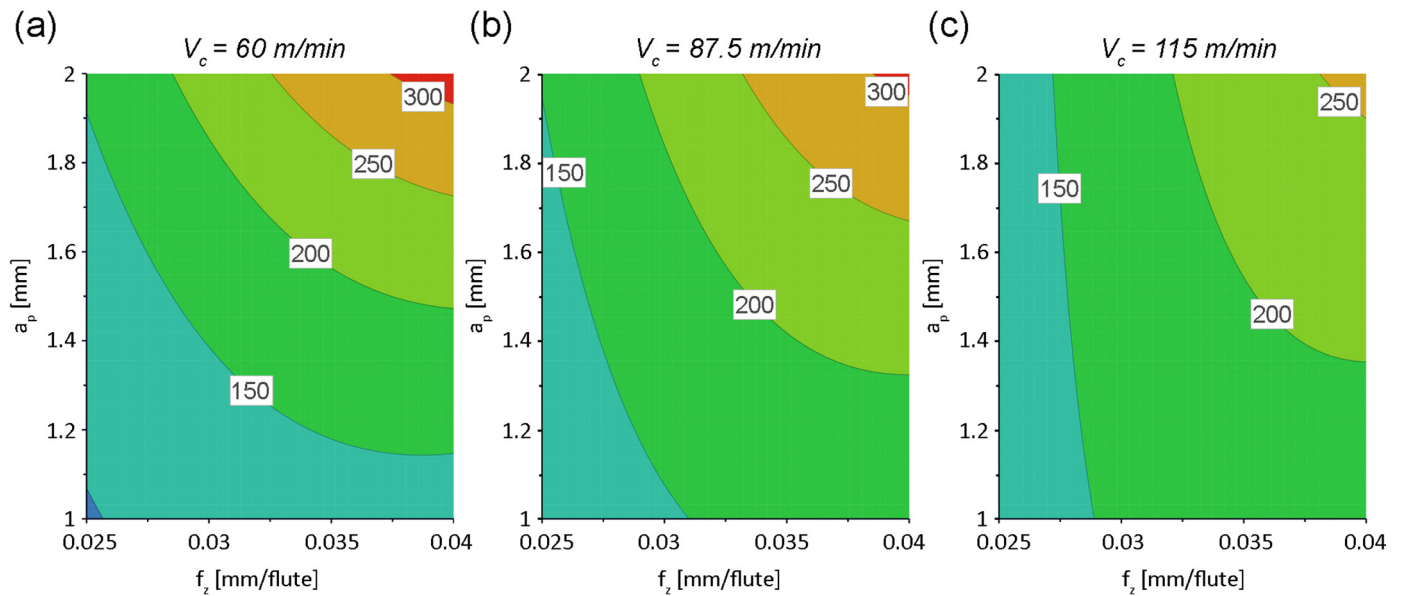
Fig. 5. 4D response contour plots of the maximum resultant cutting force in milling of CrMnFeCoNi HEA.

Fig. 8 and Fig. 9 present a comparison of tool wear in machining of both CrMnFeCoNi HEA and AISI 304L stainless steel.

The first step in establishing the tool wear model was to measure iteratively the flank wear on a tool during milling of AISI 304L stainless steel, up to a maximum wear criterion of 200 μm (Fig. 8). The tool wear trials were first carried out individually for different feeds and speeds to establish optimum cutting conditions with the requirement that the cutting time should not be less than 15 min. Once these conditions were established for AISI 304L stainless steel, the comparison experiments were performed with CrMnFeCoNi HEA. From Fig. 9(a, b), no significant in-process change in the tool flank wear was observed in machining of CrMnFeCoNi HEA. By comparison, observable progressive wear occurs along the edge of a four-flute end mill when machining stainless steel. The flank wear was not uniform over all four flutes, which resulted in a shorter tool life and could possibly affect the surface finish negatively. The insets in Fig. 9a show low magnification SEM images of the cutting edge after completion of the tool wear trials. A rapid rate of tool wear can be caused by the formation of a built up edge (BUE) on the tool due to the adhesion of test piece material to the cutting edge. The BUE is formed on the cutting edge when machining ductile materials, usually at low cutting speeds [34] and due to poor or lack of lubrication during the process. The results suggest that the adhered material can further erode the end mill's cutting edge, thus causing crater wear, which weakens the cutting edge even more and leads to a catastrophic tool failure. Yang et al. [35], also reported improved wear resistance of AlCrFeCoNi HEA compared to 304 stainless steel resulting from a high thermal and oxidative stability, enhanced by the addition of equimolar amounts of chromium and cobalt. Fig. 10 shows the tool wear from the tool top view. Higher adhesive wear was observed during machining of AISI 304L stainless steel; this is not the principal wear mode in machining of CrMnFeCoNi HEA.

The thermal conductivity of CrMnFeCoNi HEA is higher compared with stainless steel, as discussed above [36]. Applying the Coulomb friction model [31], it is assumed that all the frictional heat generated at the interface between tool and test piece is either transferred into the chip (the removed material) or conducted into the bulk. The inset SEM image in Fig. 10e shows that the wear was caused mainly by abrasion

and attrition with a low progression of tool wear during machining of CrMnFeCoNi HEA (Fig. 8).

3.3. Surface finish

The contour plots of surface roughness are shown in Fig. 11. A multiple linear regression (MRL) method was used to fit a model. The R^2 and Q^2 values were 0.818 and 0.706, respectively.

The surface roughness was most strongly affected by the feed rate, followed by the depth of cut. The cutting speed typically had a negligible influence on surface roughness in milling of CrMnFeCoNi HEA. From Fig. 11(a), it is observed that a specific combination of feed rate and axial depth of cut is needed to achieve a lower surface finish. Milling of CrMnFeCoNi HEA at various feed rates and at a middle level of depth of cut results in rougher surface. The depth of cut needs to be increased in order to minimise deflection of the end mill (higher tool stiffness) leading to a more stable process and therefore better surface finish. Higher surface roughness over the entire range of small depths of cut may be due to increased tool wear, also resulting from the combination of low depths of cut and higher feed rates. Fig. 12 shows the influence of various cutting conditions on surface topography determined by SEM image analysis.

In addition, Abbott-Firestone curves were obtained for the entire wear surface area under specific cutting conditions [37]. The histograms and cumulative distribution curves of the depths through roughness profile are shown in Fig. 12(a', f'). The roughness profile of a surface was used to calculate the average surface roughness. The R_a values are given in Fig. 12 relative to the cutting speed, feed and depth of cut. In Fig. 10(h), surface waviness can be observed at increasingly higher cutting speed during machining of CrMnFeCoNi HEA. Larger waviness is additionally produced with higher feeds regardless of the material (Fig. 12(d, i)). Therefore, the dynamic stability of the high speed end milling process becomes relatively more important than any other single factor. There was a significant difference in the depth of the roughness core profile between the two distinct materials. In Fig. 12(a', f'), the average height of the core surface for CrMnFeCoNi HEA was about half that for AISI 304L stainless steel. Characterising this behaviour is especially important for evaluating
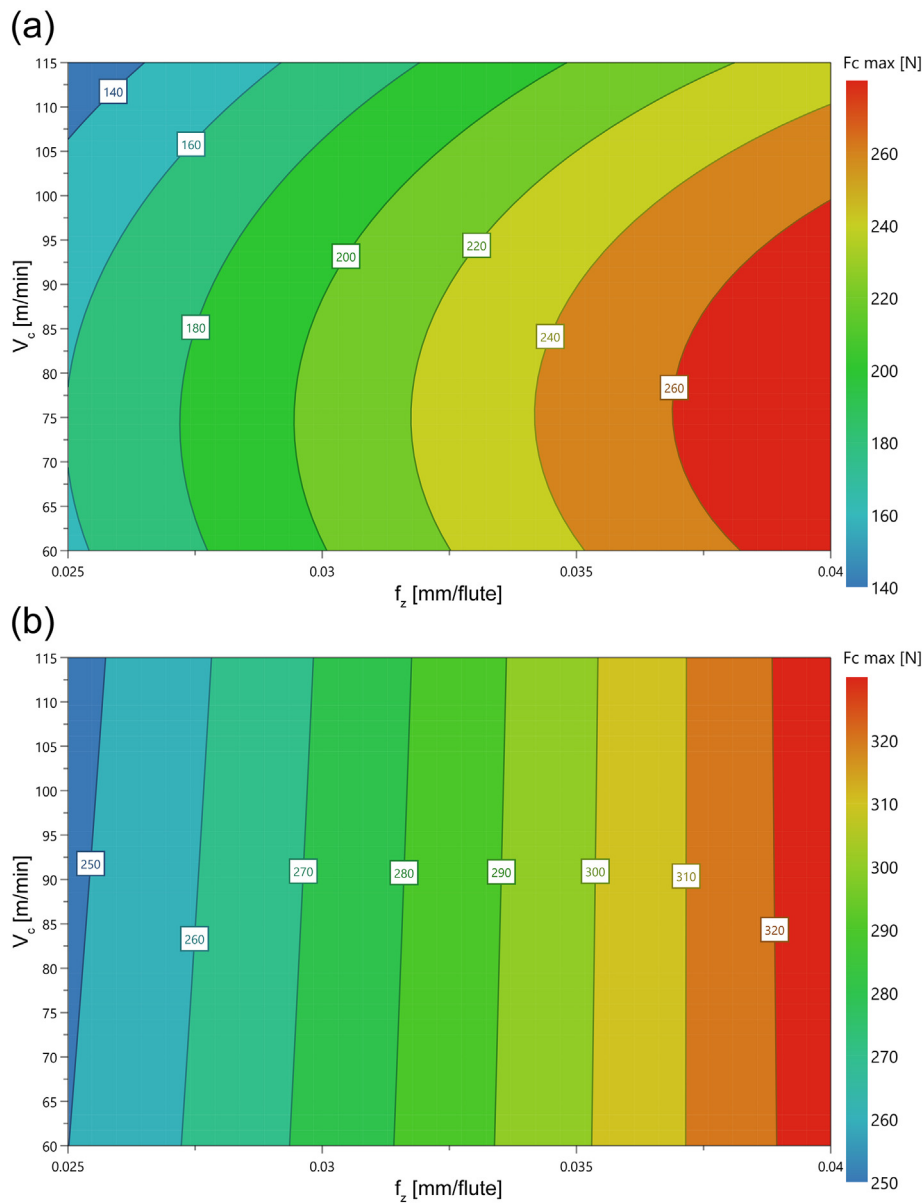
(a)

(b)

Fig. 6. 4D response contour plots of the maximum resultant force in milling of (a) CrMnFeCoNi HEA and (b) AISI 304L stainless steel, for depth of cut 2 mm. (a) CCF design (b) Full Factorial (2 levels) design as a basis for comparison only.

material's functional requirements. CrMnFeCoNi HEA could be capable of providing a low coefficient of friction and reduced wear. Therefore, it might be an important determinant of corrosion resistance of low friction materials at high temperatures [38]. Also, it can be a sufficient support for the assembly of segments [39], due to a low friction between the surfaces acting under specific load or displacement. From SEM analysis, a micro grooved surface topography was observed in CrMnFeCoNi HEA after machining. Many fine ploughing grooves can be seen in Fig. 12(f - j), validating an abrasive wear mechanism occurring during machining of CrMnFeCoNi HEA. In addition, it was also observed that abrasion of the surface, for example caused by wear debris, could deteriorate the machined surface quality at higher feed rates (Fig. 12(g, i)). It is known that ploughing causes energy to be dissipated in plastic deformation close to the machined surface [40]. It might result in higher energy requirements for the process but a lower material removal rate.

A continuous chip is most likely formed due to ploughing and elastic recovery. However, further studies are needed to explain this phenomenon. Nair et al. [41] demonstrated that ploughing is the primary mode of material removal for $Al_{0.1}CoCrFeNi$ HEA. The cutting edge radius should therefore be regarded as an important factor contributing to chip formation and surface integrity in machining of a single-phase equiatomic HEAs. In turn, shearing is the main mechanism of chip formation during machining of AISI 304L stainless steel.

Machinability of CrMnFeCoNi is good, however, further machining optimisation is required to achieve a desirable surface quality of the machined parts. The feed rate and depth of cut are the most important parameters that affect the surface finish of the CrMnFeCoNi alloy investigated here. The reasons are twofold. Firstly, CrMnFeCoNi is more ductile than AISI 304L and this causes fine-scale defects like feed marks and tearing surface, especially during machining at high feed rates.
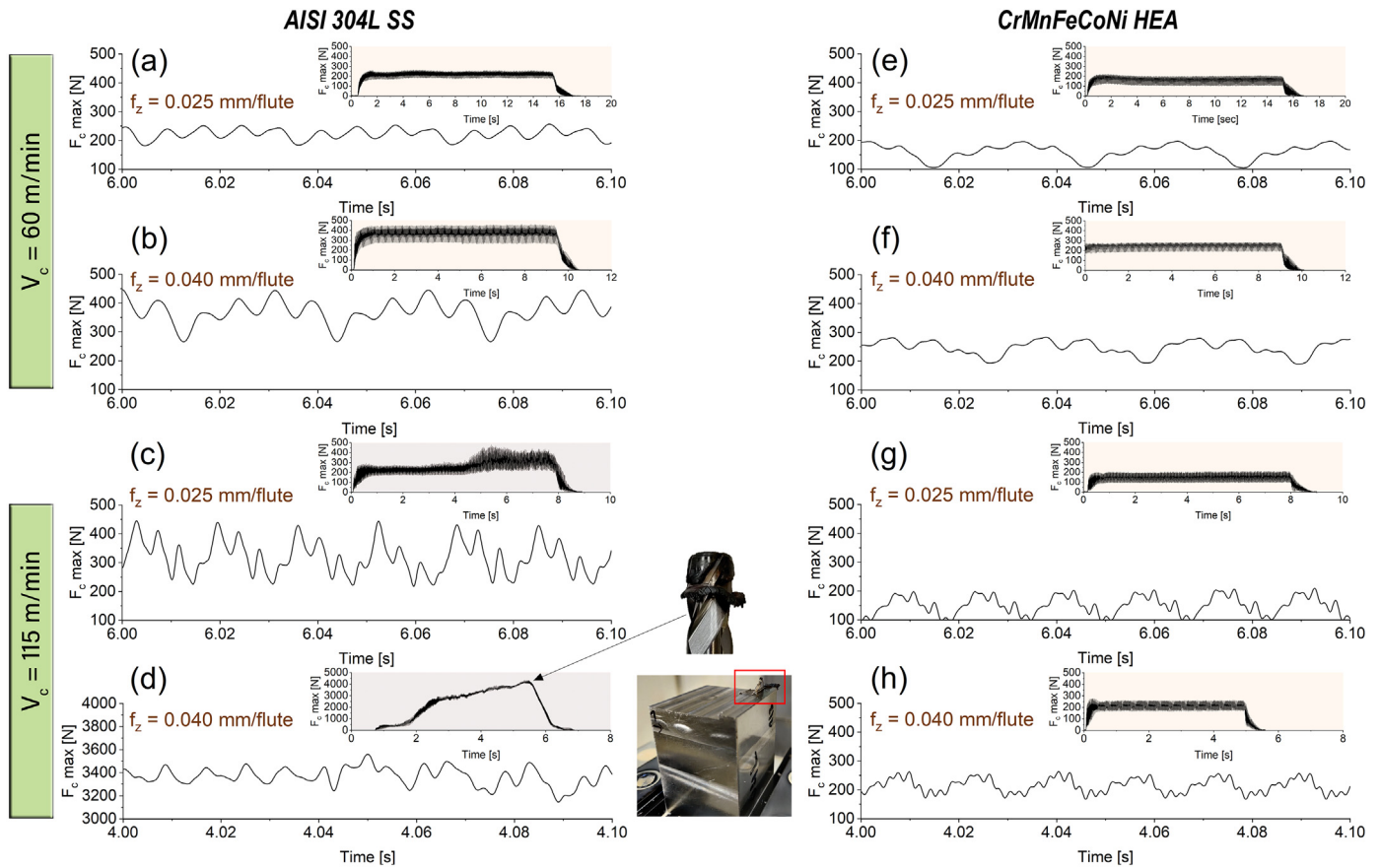
Fig. 7. The resultant cutting forces as a function of cutting time in machining of (a - d) AISI 304L stainless steel and (e - h) CrMnFeCoNi HEA.

Secondly, scaling up the manufacturing process is required for best machining practices and optimisation of cutting conditions. An axial depth of cut is a limiting factor in end milling of relatively small samples. Cutting too shallow causes tool deflection due to high cutting forces acting on the radial plane and the tool static stiffness. This results in poor surface finish and may affect a dimensional surface error, which can be critical for machining thin wall parts. Therefore, further machining optimisation is considered, after which the optimum set of parameters will be determined.

3.4. Microstructure and microhardness

Fig. 13 shows microstructural analysis of CrMnFeCoNi alloy compared to 304L stainless steel after machining.

Elemental mapping images showing the distribution of chemical elements in the HEA sample are shown on the left below in Fig. 13. To the sensitivity of the EDS analysis (15 kV) at this scale, the SLM processed CrMnFeCoNi alloy suggests that the material is of the same, uniform composition, with all elements homogeneously distributed. This corresponds to the single fcc phase discussed earlier, which was confirmed by XRD analysis (Fig. 4) and also agrees with the microstructure observations in Fig. 13. From the EDS analysis (not presented here), an overall slight depletion in Mn (16.0 at.%) compared to the chemical composition of the initial powder (19.7 at.%) was observed. This is likely to be due to its much lower vapour pressure compared to other elements, which do not evaporate as easily [42]. Further research is needed to investigate evaporation from multiphase alloys in the SLM process, and the influence of the beam parameters. Some studies have also reported that increasing the scanning speed and hatch distance can reduce evaporation losses of some elements in the SLM process of WC-Co [43]. However, changing these parameters also might reduce the density of the samples. Therefore, the necessary trade-off at the process optimisation stage needs to be performed.

From Fig. 13, it can be seen that the high feed rate affects the surface in milling of 304L. The microstructure of 304L exhibits a fully austenitic
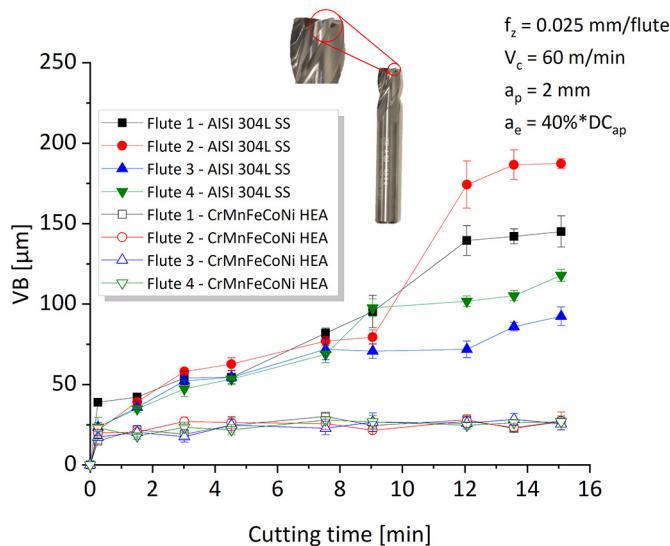

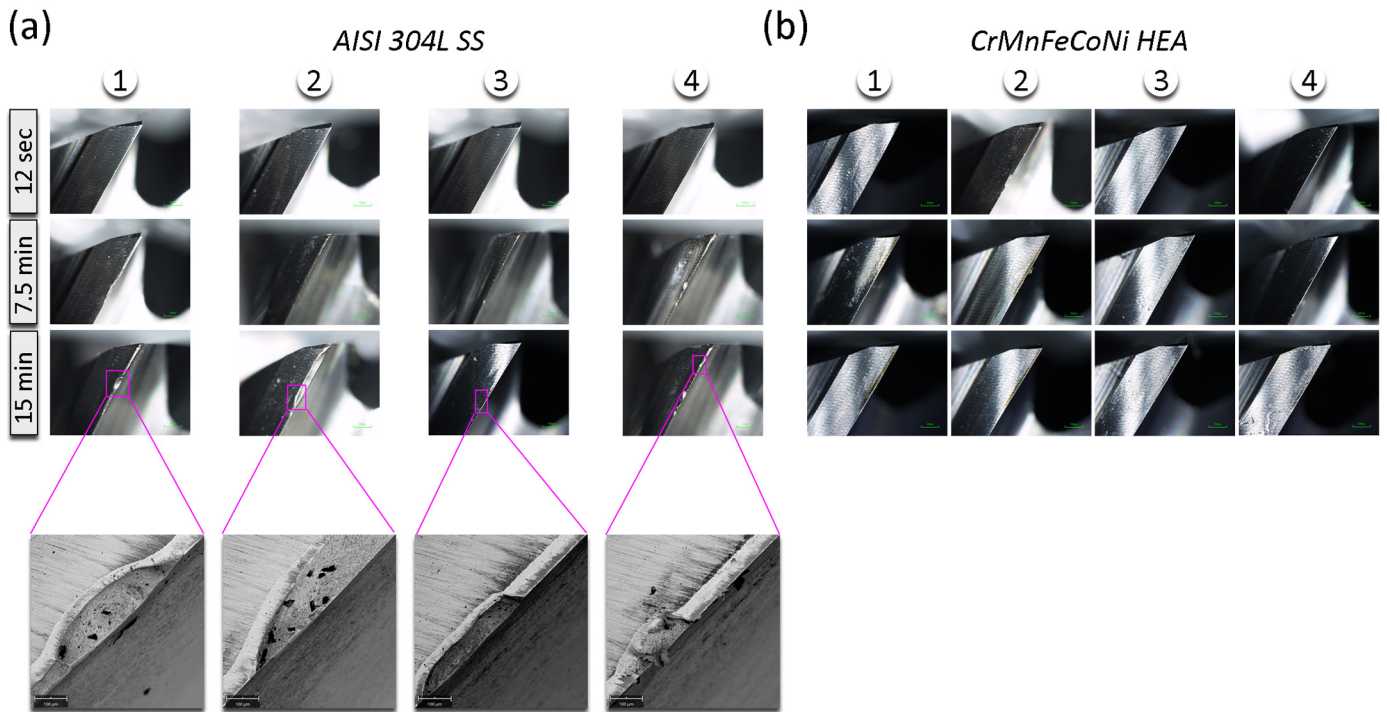
Fig. 8. Tool wear (VB) as a function of cutting time.

Fig. 9. Tool flank wear progression for a four-flute end mill in machining of (a) AISI 304L stainless steel and (b) CrMnFeCoNi HEA. SEM images in the inset (Fig. 9(a)).
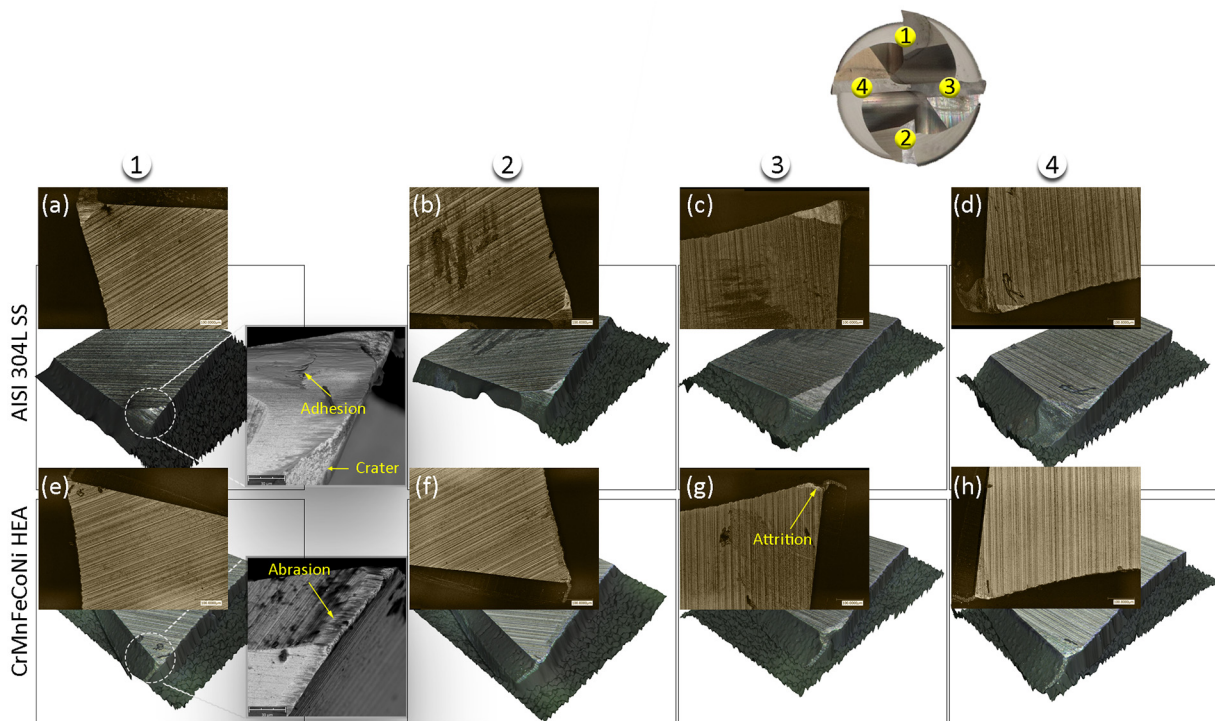

Fig. 10. Tool wear images for each flute (top view) after 15 min. of cut (V_c = 60 m/min, f_z = 0.025 mm/flute, a_p = 2 mm) in: (a - d) AISI 304L stainless steel and (e - h) CrMnFeCoNi HEA. The SEM images in the inset (Fig. 10(a, e)).
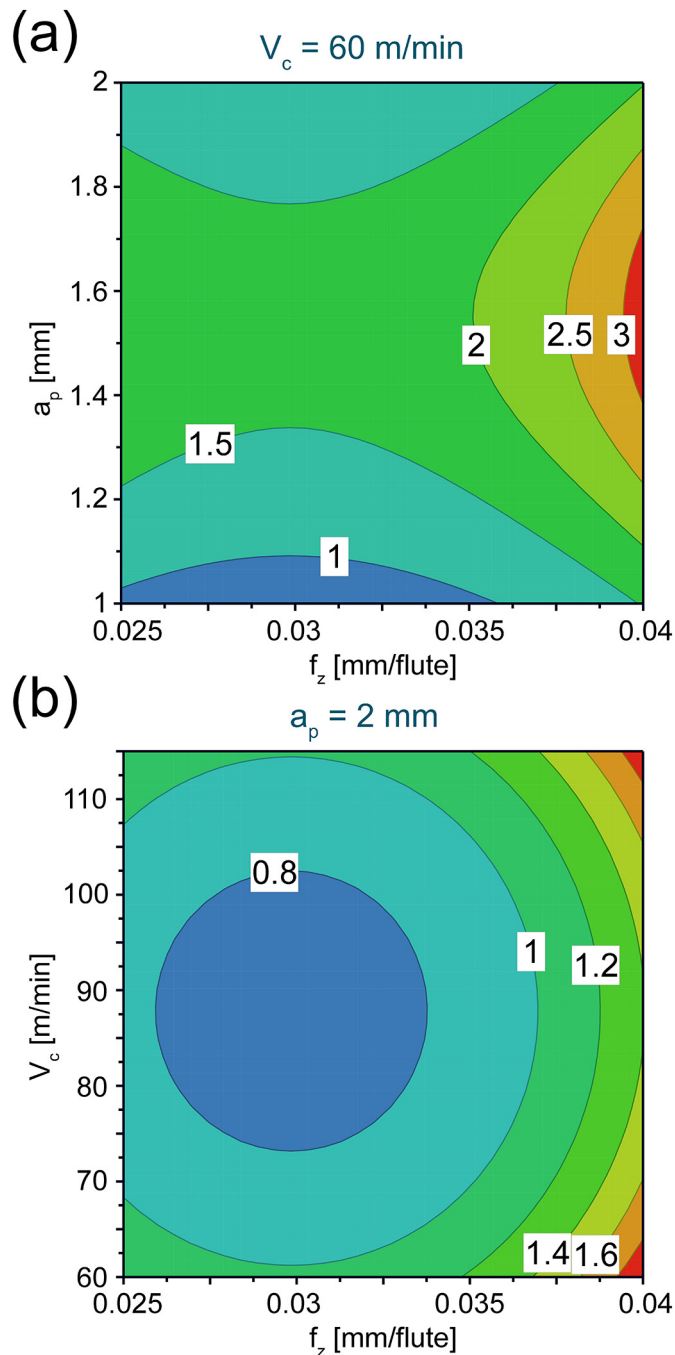
Fig. 11. Response contour plots for surface roughness as a function of (a) feed and depth of cut (V_c = 60 m/min) and (b) feed and cutting speed (a_p = 2 mm).

changes in 304L were observed at high cutting speed and feed rate. Astakhov and Shvets [44], reported that less mechanical energy is converted into thermal energy with increasing cutting speed, and that this can be sufficiently low to retain mechanical properties, which can resist permanent deformation of the machined surface. Therefore, it might be reasonably assumed that an increase in hardness near the machined surface can be achieved by increasing feed rate, and at low cutting speed. This was investigated further by microhardness analysis. The results are presented in Fig. 14.

To fully understand the microstructural development in the near-surface region as a result of the machining process, EBSD was performed on cross sections of samples of both the CrMnFeCoNi and 304L, both machined at V_c = 60 m/min and f_z = 0.040 mm/flute (therefore corresponding to the conditions of (b) and (g) in Fig. 13, and the hardness profiles in Fig. 14). Fig. 15 shows the inverse pole figure (IPF) orientation maps for each and highlights the local misorientation distribution maps.

Firstly, the images in Fig. 15 give information on the microstructure of each alloy. Away from the machined surface the 304L SS shows an equiaxed grain structure with a number of annealing twins. The CrMnFeCoNi on the other hand shows a more columnar microstructure, as would be typical of an AM-processed alloy [45]. Looking at the machined surface in more detail, the misorientation maps show a clear difference between the two samples, where the 304L SS only shows orientation difference (introduced by the deformation of the machining operation) in the near surface region (to about 20 μm depth), and the orientation differences in this zone are large. In the CrMnFeCoNi on the other hand the misorientation is spread to a much larger depth, over 100 μm. This may be a sign that the deformation strain on the surface caused by the machining operation has been relieved by transferring the strain to internal areas, though high local misorientation can be observed in samples produced by AM, due to the thermal cycling that the material experiences during processing. Nevertheless, the intensity of local misorientation beneath the machined surface (as well as the Geometrically Necessary Dislocation Density, explored later) is lower in CrMnFeCoNi than in 304L SS, which arguably suggests that it is due to strain transfer, rather than being retained from processing. It should also be noticed that deformation twins were only introduced by machining in the 304L SS sample (as indicated by the white arrows shown in Fig. 15(a)).

The EBSD data can be further used to explore whether the difference in structure and texture in the starting material would be expected to lead to a difference in behaviour in its own right, setting aside the difference in alloy composition, and also to investigate dislocation activity which is associated with the misorientation. Fig. 16 shows the Schmid factor map, which will indicate if either sample shows a hard or soft orientation along the external cutting force when considering the easily activated slip system ($\{111\} < 1\bar{1}0>$) in FCC structured materials, created for each of the imaged zones from Fig. 15, and also a map generated showing the density of Geometrically Necessary Dislocations (GNDs) across the same regions. The Schmid factor map (Fig. 16 (a,b)) shows no evident difference for the Schmid factor distribution for the analysed slip system ($\{111\} < 1\bar{1}0>$), indicating that, despite the oriented microstructure of the CrMnFeCoNi, an orientation effect on deformation would not be expected. The GND maps collected from the very top near surfaces of two samples (Fig. 16 (c, d)) show, as would be expected, that the regions of high misorientation in Fig. 15 correspond to high areas of GND activity. Fig. 16 (e, f) shows the GND chart of these two samples and it is clear that GND density of the CrMnFeCoNi is lower than the 304L SS.

From the EBSD results in general, there is a noticeable tendency for high dislocation densities which is consistent with the observation of the existence of cellular dislocation substructures in the columnar grains formed in Additively Manufactured HEAs [46,47]. Dislocation cells could have an effect on the machinability characteristics of additively manufactured alloys of this type by changing the mechanical
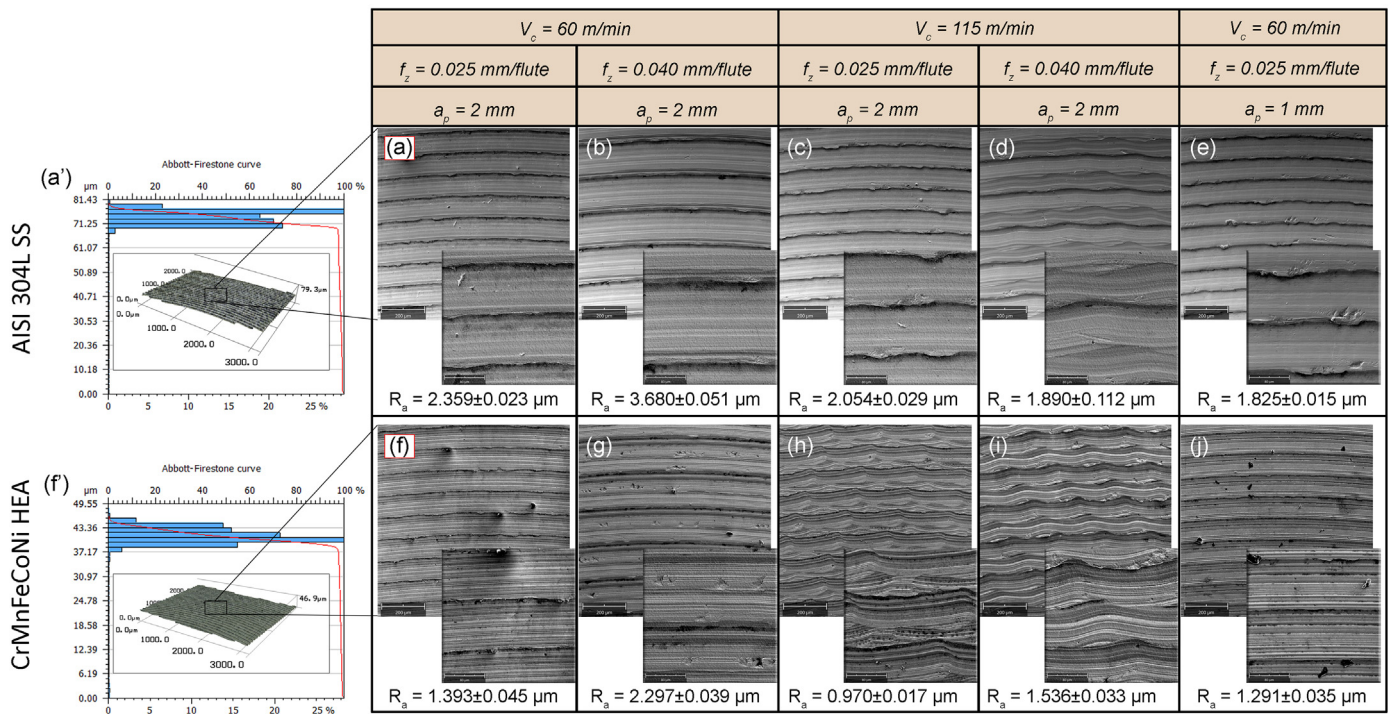
structure with a non-homogeneously distributed coarse phase (δ-ferrite). Some subsurface alterations were observed by using high tool feed rate and lower cutting speed, which resulted in considerable plastic deformation in 304L material (Fig. 13(b)). This indicates increased cutting temperature, because of increased friction and tool wear at high feed rates. No significant cross-sectional microstructural changes were observed in CrMnFeCoNi HEA, regardless of the cutting conditions being used (Fig. 13(f - j)). Microstructural observations are also consistent with the results of the surface roughness and hardness measurements. Higher surface roughness was observed at increased feed rate and lower cutting speed when machining both the HEA and reference steel, comparing different cutting conditions (Fig. 12(b, g)). In Fig. 13(d), no microstructural

Fig. 12. (a – j) SE-SEM images of surface finish with the main surface defects at higher (1000×) magnification (insets). (a', f') Quantitative characterisation of surface topography with the Abbott-Firestone curves.
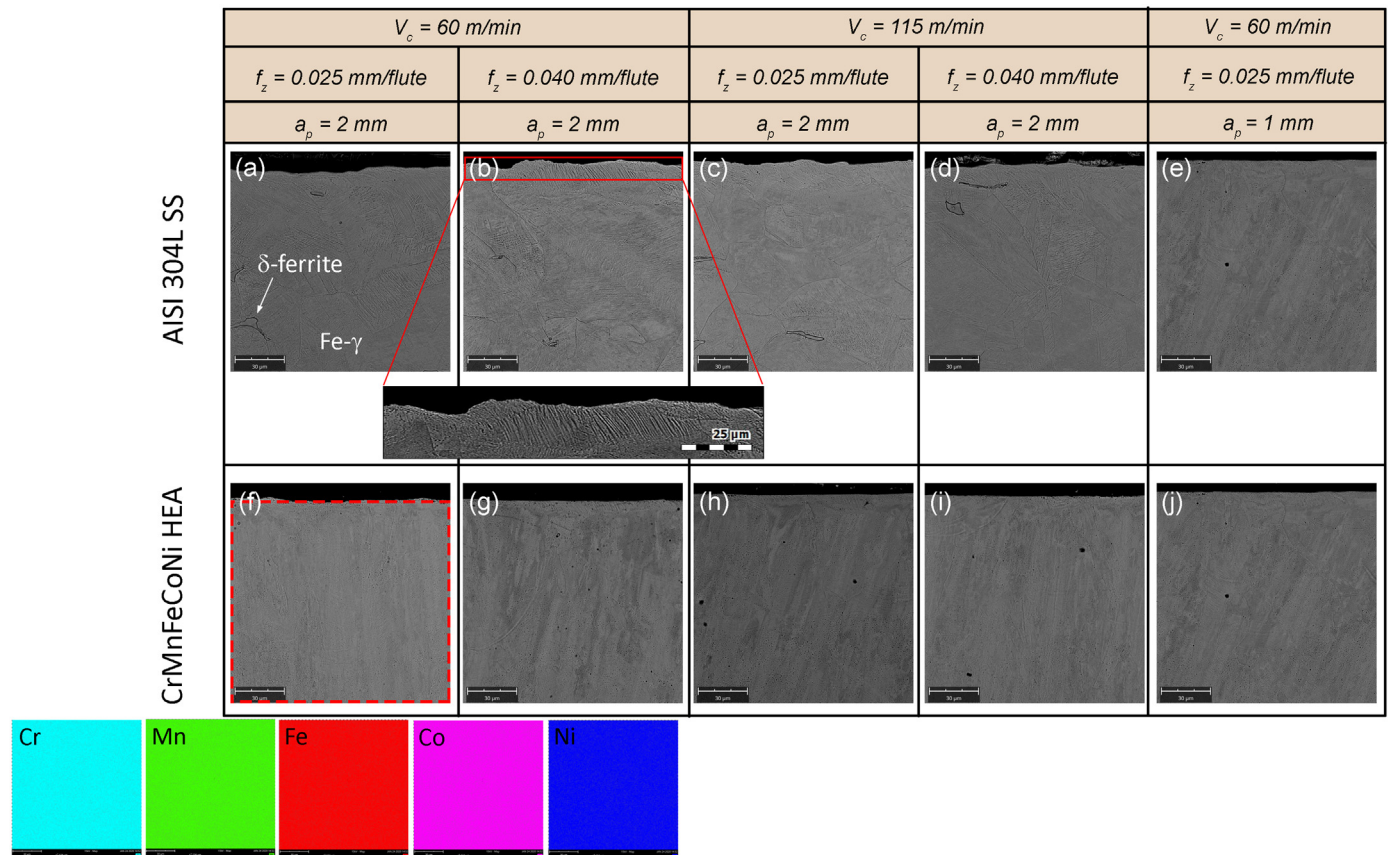

Fig. 13. Cross-sectional SEM micrographs (Mag. 2000×) of the samples: (a – e) AISI 304L SS and (f – j) CrMnFeCoNi HEA after machining with different cutting conditions. EDS map (inset in f).
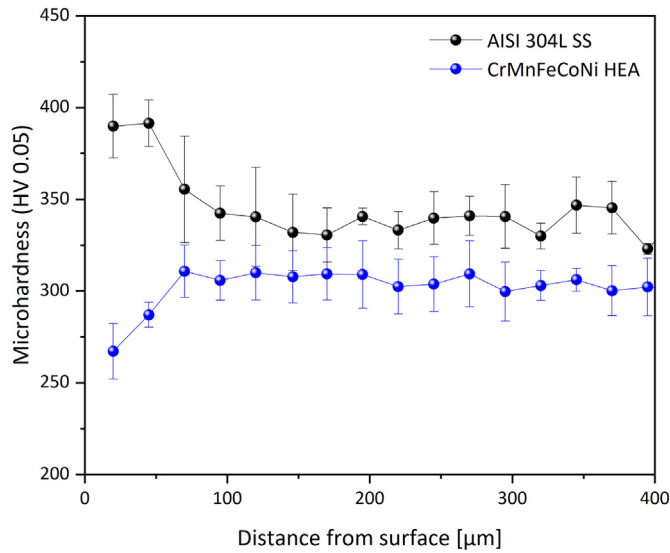
Fig. 14. Cross-sectional microhardness profile for AISI 304L SS and CrMnFeCoNi HEA machined at $V_c = 60$ m/min and $f_z = 0.040$ mm/flute.

machining process itself influencing the grain structure. To shed light on this process further investigations would be needed, but with the data here it is possible to make some initial inferences about the effects with relevance to machining.

Exploring the differences between the machined surface and the material further away from this surface in Fig. 16 (which shows the cross section) suggests an increase in misorientation and, to some extent, the dislocation density in the region of the surface, particularly for 304L. This could indicate strain hardening of the surface of 304L from machining. In the CrMnFeCoNi alloy, the deformation strain seems to be more easily transferred to the deeper interior of the material. Based on the available data [50], equiatomic CrMnFeCoNi HEA shows a high strain hardening rate, especially at low temperatures (which could perhaps be generally compared to the behaviour at the high strain rates experienced in machining), due to mechanical twinning. Although micro-sized deformation twins can be found in the 304L SS sample in the grain near the machined surface, no evidence of deformation twins was observed in the CrMnFeCoNi alloy sample. We also note that in some reports of twinning in the CrMnFeCoNi alloy, the twins formed are nanoscale, and so may not have been observed in our imaging [51]. It appears that the alloy does have the ability to distribute strain further into the structure than the 304L sample, and thus avoid the concentration of work hardening and increase in hardness seen in Fig. 13. The softening behaviour at this could be associated with the dynamic recovery process [52], either due to shear localisation (which can be associated with thermal softening when crystallographic planes tend to orient in desirable directions for slip as a response to the strain), or simply through a thermal mechanism. In relation to the latter, it should be noted that as-produced AM parts may have a relatively high dislocation density to begin with, due to the residual stresses in manufacture. Further investigation of these effects, including Transmission Electron Microscopy to understand the dislocation processes occurring and a detailed analysis of shear localisation and local strain transfer in HEA are required to better understand the deformation mechanism of HEA during machining.
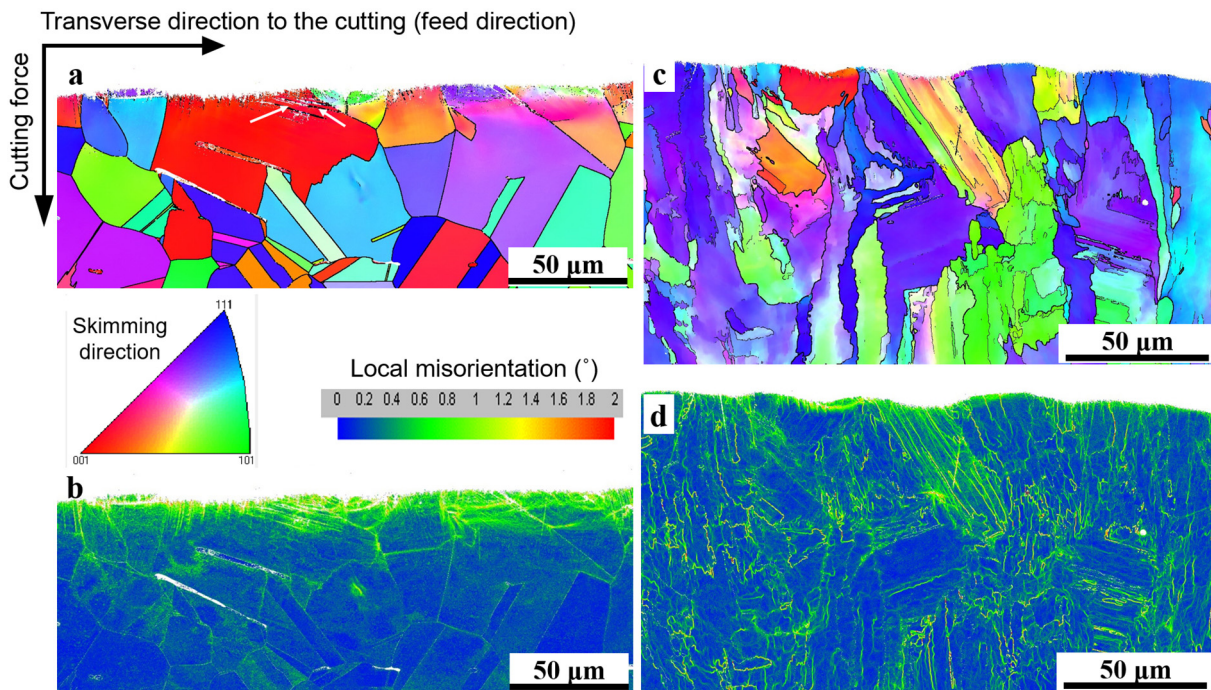
response of the material and causing strengthening. Zhu et al. [46] have noted that the dislocation substructures can be removed by heat treatment, and they could therefore be affected by the machining conditions. It has also been observed that the substructures can change configuration at high strains, from regular dislocation cells to localised dislocation clusters (dependant on grain size and precipitation) [48], and it is possible that dynamic recovery could occur. Grain refinement is also an observed mechanism for strength enhancement in HEAs [48,49], and one that could affect the response of a material to machining, though alternations to its deformation characteristics. As for dislocation substructures, the effect of grain size in the present case could be complex, with the possibility of thermal or high strain effects due to the

Fig. 15. EBSD Inverse Pole Figure (IPF) orientation maps and local misorientation derived from EBSD measurements for (a, b) AISI 304L SS and (c, d) CrMnFeCoNi HEA machined at $V_c = 60$ m/min and $f_z = 0.040$ mm/flute.
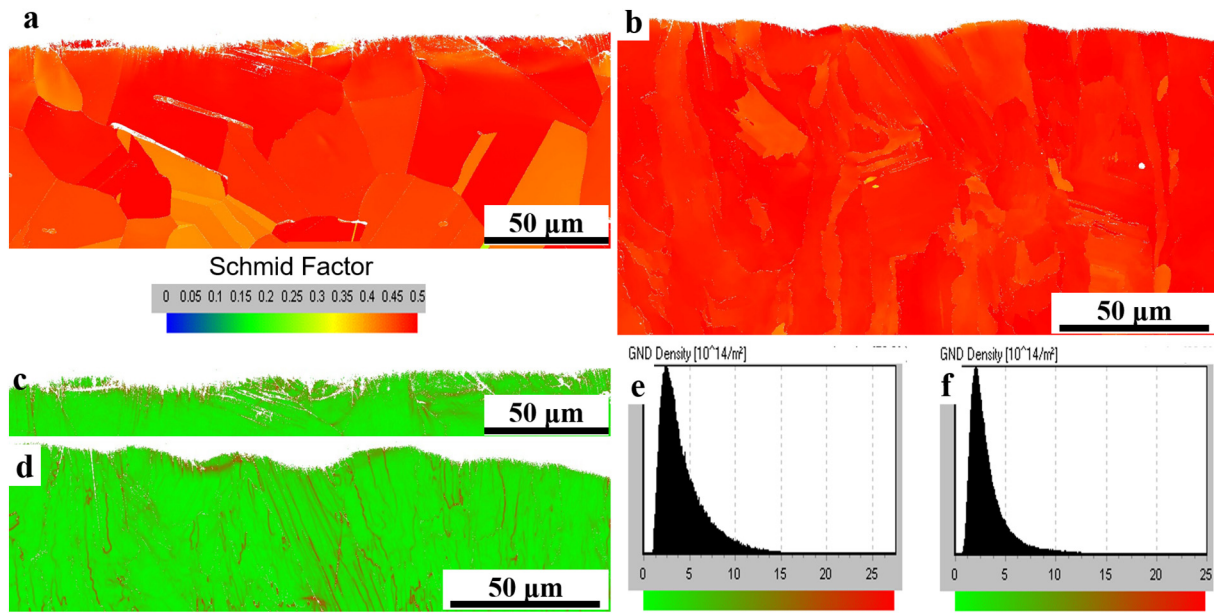
Fig. 16. Schmid factor and Geometrically Necessary Dislocation density maps derived from EBSD measurements for cross sections from the machined surface in samples of AISI 304L SS and CrMnFeCoNi HEA machined at $V_c = 60$ m/min and $f_z = 0.040$ mm/flute. (a,b) Schmid factor (($\{111\} < 1\bar{1}0>$) slip system), for 304L and CrMnFeCoNi respectively, (c,d) GND maps for 304L and CrMnFeCoNi respectively and (e,f) GND distribution charts derived from EBSD measurements for 304L and CrMnFeCoNi respectively.

4. Conclusions

This study has found optimised processing parameters for the SLM Additive Manufacture of CrMnFeCoNi, and has used these to create a relatively large block (around $50 \times 50 \times 50$ mm) of the material. The machining characteristics of this block first indicate that the processing has achieved good homogeneity in the material (through the analysis of the force-feedback signal), but also demonstrates that the machining of this HEA alloy in this form is possible. Furthermore, the machining conditions design space has been explored and optimised cutting conditions appropriate to process the alloy were found. The tool wear results were compared to 304L stainless steel, indicating an improved machinability of the HEA. The 304L shows work hardening near the surface, with the HEA shows surface softening. This is due to the CrMnFeCoNi being able to accommodate strain deeper into the surface and seeing less concentrated work hardening, while a softening mechanism, either thermal or due to a shear transformation, operates. This significantly reduces tool wear while not affecting the strength of the alloy. While it is unlikely that the same behaviour occurs in all HEAs, the results demonstrate that HEAs with good machinability can be found, and that particular behaviours inherent to some of these compositions can offer new routes to achieving good machinability characteristics.

Data availability

The raw/processed data required to reproduce these findings can not be shared at this time as the data also forms part of an ongoing study.

Declaration of Competing Interest

The authors declare that they have no known competing financial interests or personal relationships that could have appeared to influence the work reported in this paper.

Acknowledgements

References

[1] E.P. George, W.A. Curtin, C.C. Tasan, High entropy alloys: a focused review of mechanical properties and deformation mechanisms, Acta Mater. 188 (2020) 435–474.

[2] E.J. Pickering, N.G. Jones, High-entropy alloys: a critical assessment of their founding principles and future prospects, Int. Mater. Rev. 61 (2016) 183–202.

[3] D.B. Miracle, J.D. Miller, O.N. Senkov, C. Woodward, M.D. Uchic, J. Tiley, Exploration and development of high entropy alloys for structural applications, Entropy 16 (2014) 494–525.

[4] D.B. Miracle, O.N. Senkov, A critical review of high entropy alloys and related concepts, Acta Mater. 122 (2017) 448–511.

[5] Y.F. Ye, Q. Wang, J. Lu, C.T. Liu, Y. Yang, High-entropy alloy: challenges and prospects, Mater. Today 19 (2016) 349–362.

[6] E.P. George, D. Raabe, R.O. Ritchie, High-entropy alloys, Nat. Rev. Mater. 4 (2019) 515–534.

[7] Z. Li, S. Zhao, R.O. Ritchie, M.A. Meyers, Mechanical properties of high-entropy alloys with emphasis on face-centered cubic alloys, Prog. Mater. Sci. 102 (2019) 296–345.

[8] G. Bracq, M. Laurent-Brocq, L. Perriere, R. Pires, J.-M. Joubert, I. Guillot, The fcc solid solution stability in the Co-Cr-Fe-Mn-Ni multi-component system, Acta Mater. 128 (2017) 327–336.

[9] B. Cantor, I.T.H. Chang, P. Knight, A.J.B. Vincent, Microstructural development in equiatomic multicomponent alloys, Mater. Sci. Eng. A 375-377 (2004) 213–218.

[10] N.N. Kumbhar, A.V. Mulay, Post processing methods used to improve surface finish of products which are manufactured by additive manufacturing technologies: a review, J. Instit. Eng.(India): Seri. C 99 (2018) 481–487.

[11] O. Oyelola, P. Crawforth, R. M'Saoubi, A.T. Clare, Machining of additively manufactured parts: implications for surface integrity, Procedia CIRP 45 (2016) 119–122.

[12] G. Laplanche, S. Berglund, C. Reinhart, A. Kostka, F. Fox, E.P. George, Phase stability and kinetics of σ-phase precipitation in CrMnFeCoNi high-entropy alloys, Acta Mater. 161 (2018) 338–351.

[13] Z. Huang, Y. Dai, Z. Li, G. Zhang, C. Chang, J. Ma, Investigation on surface morphology and crystalline phase deformation of Al80Li5Mg5Zn5Cu5 high-entropy alloy by ultra-precision cutting, Mater. Des. 186 (2020) 108367.

[14] I. Kunce, M. Polanski, K. Karczewski, T. Plocinski, K.J. Kurzydlowski, Microstructural characterisation of high-entropy alloy AlCoCrFeNi fabricated by laser engineered net shaping, J. Alloys Compd. 648 (2015) 751–758.

[15] Z. Tong, X. Ren, J. Jiao, W. Zhou, Y. Ren, Y. Ye, E.A. Larson, J. Gu, Laser additive manufacturing of FeCrCoMnNi high-entropy alloy: effect of heat treatment on microstructure, residual stress and mechanical property, J. Alloys Compd. 785 (2019) 1144–1159.

[16] P. Chen, S. Li, Y. Zhou, M. Yan, M.M. Attallah, Fabricating CoCrFeMnNi high entropy alloy via selective laser melting in-situ alloying, J. Mater. Sci. Technol. 43 (2020) 40–43.

[17] R. Sokkalingam, K. Sivaprasad, M. Duraiselvam, V. Muthupandi, K.G. Prashanth, Novel welding of Al0.5CoCrFeNi high-entropy alloy: Corrosion behavior, J. Alloys Compd. 817 (2020) 153163.

[18] F. Zheng, G. Zhang, X. Chena, X. Yang, Z. Yang, Y. Li, A new strategy of tailoring strength and ductility of CoCrFeNi based high-entropy alloy, Mater. Sci. Eng. A 774 (2020) 138940.

[19] J. Guo, C. Tang, G. Rothwell, L. Li, Y.-C. Wang, Q. Yang, X. Ren, Welding of high entropy alloys - a review, Entropy 21 (2019) 431.

[20] E. Hosseinia, V.A. Popovich, A review of mechanical properties of additively manufactured Inconel 718, Addit. Manufact. 30 (2019) 100877.

[21] D. Zhu, X. Zhang, H. Ding, Tool wear characteristics in machining of nickel-based superalloys, Int. J. Mach.Tools Manufact. 64 (2013) 60–77.

[22] P.S. Gowthaman, S. Jeyakumar, B.A. Saravanan, Machinability and tool wear mechanism of duplex stainless steel - a review, Mater. Today: Proce. 26 (2020) 1423–1429.

[23] T. Childerhouse, E. Hernandez-Nava, R. M'Saoubi, N. Tapoglou, M. Jackson, Surface and sub-surface integrity of Ti-6Al-4V components produced by selective electron beam melting with post-build finish machining, Procedia CIRP 87 (2020) 309–314.

[24] W. Mycroft, M. Katzman, S. Tammes-Williams, E. Hernandez-Nava, G. Panoutsos, I. Todd, V. Kadirkamanathan, A data-driven approach for predicting printability in metal additive manufacturing processes, J. Intell. Manuf. 31 (2020) 1769–1781.

[25] ISO 8688-2, Tool Life Testing in Milling - Part 2: End Milling, 1989.

[26] I. Unanue, J. Díaz, F. Garciandia, M.S. Sebastian, A.M. Mancisidor, P. Alvarez, Reduction of the residual porosity in parts manufactured by selective laser melting using skywriting and high focus offset strategies, Phys. Procedia 83 (2016) 864–873.

[27] C.L.A. Leung, S. Marussi, M. Towrie, J. del Val Garcia, R.C. Atwood, A.J. Bodey, J.R. Jones, P.J. Withers, P.D. Lee, Laser-matter interactions in additive manufacturing of stainless steel SS316L and 13-93 bioactive glass revealed by in situ X-ray imaging, Addit. Manufact. 24 (2018) 647–657.

[28] M. Thomas, G.J. Baxter, I. Todd, Normalised model-based processing diagrams for additive layer manufacture of engineering alloys, Acta Mater. 108 (2016) 26–35.

[29] Y. Brif, M. Thomas, I. Todd, The use of high-entropy alloys in additive manufacturing, Scr. Mater. 99 (2015) 93–96.

[30] R. Li, P. Niu, T. Yuan, P. Cao, C. Chen, K. Zhou, Selective laser melting of an equiatomic CoCrFeMnNi high-entropy alloy: Processability, non-equilibrium microstructure and mechanical property, J. Alloys Compd. 746 (2018) 125–134.

[31] M. Nasr, E.-G. Ng, M. Elbestawi, Effects of workpiece thermal properties on machining-induced residual stresses - thermal softening and conductivity, Proc. Inst. Mech. Eng. B J. Eng. Manuf. 221 (2007) 1387–1400.

[32] K. Jin, B.C. Sales, G.M. Stocks, G.D. Samolyuk, M. Daene, W.J. Weber, Y. Zhang, H. Bei, Tailoring the physical properties of Ni-based single-phase equiatomic alloys by modifying the chemical complexity, Sci. Rep. 6 (2016) 20159.

[33] C.S. Kim, Thermophysical Properties of Stainless Steel, Argonne, Argonne National Laboratory, 1975.

[34] N. Fang, P. Srinivasa Pai, S. Mosquea, The effect of built-up edge on the cutting vibrations in machining 2024-T351 aluminum alloy, Int. J. Adv. Manuf. Technol. 49 (2010) 63–71.

[35] S. Yang, Z. Liu, J. Pi, Microstructure and wear behavior of the AlCrFeCoNi high-entropy alloy fabricated by additive manufacturing, Mater. Lett. 261 (2020) 127004.

[36] Ke Jin, Hongbin Bei, Single-phase concentrated solid-solution alloys: bridging intrinsic transport properties and irradiation resistance, Front. Mater. 5 (2018) 1–11.

[37] ISO 13565-2, Geometrical Product Specifications (GPS) - Surface Texture: Profile Method; Surfaces Having Stratified Functional Properties - Part 2: Height Characterization using the Linear Material Ratio Curve, 1996.

[38] R.N. Johnson, R.C. Aungst, N.J. Hoffman, M.G. Cowgill, G.A. Whitlow, W.L. Wilson, Development of Low Friction Materials for LMFBR Components (CONF-760503–P1), United States 1976.

[39] K.F. Nilsson, Assessment of thin-walled cladding tube mechanical properties by segmented expanding Mandrel test, Structural Materials for Innovative Nuclear Systems (SMINS-3), Idaho Falls, 2013.

[40] B. Bhushan, Modern Tribology Handbook, CRC Press, Ohio, 2000.

[41] R.B. Nair, H.S. Arora, A. Ayyagari, S. Mukherjee, H.S. Grewal, High entropy alloys: Prospective materials for tribo-corrosion applications, Adv. Eng. Mater. 20 (2018).

[42] David R. Lide (Ed.), CRC Handbook of Chemistry and Physics, 84th Edition; Section 4, Properties of the Elements and Inorganic Compounds; Vapor Pressure of the, CRC Press, Metallic Elements, Boca Raton, Florida, 2003.

[43] E. Uhlmann, A. Bergmann, W. Gridin, Investigation on additive manufacturing of tungsten carbide-cobalt by selective laser melting, Procedia CIRP 35 (2015) 8–15.

[44] V.P. Astakhov, S. Shvets, The assessment of plastic deformation in metal cutting, J. Mater. Process. Technol. 146 (2004) 193–202.

[45] A.A. Antonysamy, J. Meyer, P.B. Prangnell, Effect of build geometry on the β-grain structure and texture in additive manufacture of Ti6Al4V by selective electron beam melting, Mater. Charact. 84 (2013) 153–168.

[46] Z.G. Zhu, Q.B. Nguyen, F.L. Ng, X.H. An, X.Z. Liao, P.K. Liaw, S.M.L. Nai, J. Wei, Hierarchical microstructure and strengthening mechanisms of a CoCrFeNiMn high entropy alloy additively manufactured by selective laser melting, Scr. Mater. 154 (2018) 20–24.

[47] M. Song, R. Zhou, J. Gu, Z. Wang, S. Ni, Y. Liu, Nitrogen induced heterogeneous structures overcome strength-ductility trade-off in an additively manufactured high-entropy alloy, Appl. Mater. Today 18 (2020) 100498.

[48] Z. Wang, I. Baker, W. Guo, J.D. Poplawsky, The effect of carbon on the microstructures, mechanical properties, and deformation mechanisms of thermo-mechanically treated $Fe_{40.4}Ni_{11.3}Mn_{34.8}Al_{7.5}Cr_6$ high entropy alloys, Acta Mater. 126 (2017) 346–360.

[49] J.Y. He, H. Wang, H.L. Huang, X.D. Xu, M.W. Chen, Y. Wu, X.J. Liu, T.G. Nieh, K. An, Z.P. Lu, A precipitation-hardened high-entropy alloy with outstanding tensile properties, Acta Mater. 102 (2016) 187–196.

[50] M.J. Jang, D.-H. Ahn, J. Moon, J.W. Bae, D.Y. Jien-Wei, Constitutive modeling of deformation behavior of high-entropy alloys with face-centered cubic crystal structure, Mater. Res. Lett. 5 (2017) 350–356.

[51] B. Gludovatz, A. Hohenwarter, D. Catoor, E.H. Chang, E.P. George, R.O. Ritchie, A fracture-resistant high-entropy alloy for cryogenic applications, Science 345 (2014) 1153–1158.

[52] T. Liu, Z. Wu, A.D. Stoica, Q. Xie, W. Wu, Y. Gao, H. Bei, K. An, Twinning-mediated work hardening and texture evolution in CrCoFeMnNi high entropy alloys at cryogenic temperature, Mater. Des. 131 (2017) 419–427.